

REPORT DOCUMENTATION PAGE**Form Approved**
OMB No. 0704-0188

Public reporting burden for this collection of information is estimated to average 1 hour per response, including the time for reviewing instructions, searching data sources, gathering and maintaining the data needed, and completing and reviewing the collection of information. Send comments regarding this burden estimate or any other aspect of this collection of information, including suggestions for reducing this burden to Washington Headquarters Service, Directorate for Information Operations and Reports, 1215 Jefferson Davis Highway, Suite 1204, Arlington, VA 22202-4302, and to the Office of Management and Budget, Paperwork Reduction Project (0704-0188) Washington, DC 20503.

PLEASE DO NOT RETURN YOUR FORM TO THE ABOVE ADDRESS.**1. REPORT DATE (DD-MM-YYYY)**

03-01-2012

2. REPORT TYPE

Final

3. DATES COVERED (From - To)

April 1, 2009 - November 20, 2011

4. TITLE AND SUBTITLE

Optoelectronics Research Center

5a. CONTRACT NUMBER**5b. GRANT NUMBER**

FA9550-09-1-0202

5c. PROGRAM ELEMENT NUMBER**6. AUTHOR(S)**

Steven R. J. Brueck

5d. PROJECT NUMBER**5e. TASK NUMBER****5f. WORK UNIT NUMBER****7. PERFORMING ORGANIZATION NAME(S) AND ADDRESS(ES)**University of New Mexico
Center for High Technology Materials
1313 Goddard SE
Albuquerque, NM 87106**8. PERFORMING ORGANIZATION
REPORT NUMBER****9. SPONSORING/MONITORING AGENCY NAME(S) AND ADDRESS(ES)**Dr. Howard Schlossberg
AFOSR/NE
801 N. Randolph St.
Arlington, VA 22203-1977**10. SPONSOR/MONITOR'S ACRONYM(S)**
AFOSR/NE**11. SPONSORING/MONITORING
AGENCY REPORT NUMBER**

AFRL-OSR-VA-TR-2012-0722

12. DISTRIBUTION AVAILABILITY STATEMENT

Unlimited Public Availability

13. SUPPLEMENTARY NOTES**14. ABSTRACT**

Research performed at the University of New Mexico under the AFOSR-supported optoelectronics Research Center is reported. This includes work on: high temperature nanoparticle phosphors, optomechanical oscillators, GaN nanoepitaxial growth and devices, dual-wavelength IR lasers for THz generation, CVD diamond and VECSEL integration, plasmonic detectors and focal plane arrays, and 3D interferometric lithography.

15. SUBJECT TERMS

quantum dot lasers, THz sources, nanoparticles, phosphors, optomechanics, GaN, nanoepitaxy, VECSEL, 3D lithography, QDIP, focal plane array

16. SECURITY CLASSIFICATION OF:**a. REPORT****b. ABSTRACT****c. THIS PAGE****17. LIMITATION OF
ABSTRACT****18. NUMBER
OF PAGES**
45**19a. NAME OF RESPONSIBLE PERSON**

Steven R. J. Brueck

19b. TELEPHONE NUMBER (Include area code)

505-272-7800

Abstract	3
Introduction	3
1. ZnSe:Mn/ZnS High Temperature Nanophosphors with Very High Quantum Efficiency for White LEDs (Osinski)	3
2. Harmonic RF frequency generation in optomechanical oscillator (OMOs) (Hossein-Zadeh)	6
3. Optical control of microwave networks using bulk effects (Hossein-Zadeh)	7
4. Developing waveguides for on-chip integration of high-Q silica microtoroids (Hossein-Zadeh)	9
5. Hybrid optomechanical resonator (Hossein-Zadeh)	10
6. GaN Growth and Devices (Hersee)	11
7. Dual Wavelength QD Sources for THz Generation (Lester)	15
8. CVD diamond and VECSEL integration (Balakrishnan).	19
9. Quantum dot VECSELs. (Balakrishnan)	20
10. Plasmonic fluorophores (Jain)	22
11. Plasmonic Tunnel Junctions (Jain):	24
12. Advanced Microstructured Fibers (Jain)	25
13. Plasmonic Infrared Detectors and Focal Plane Arrays (Brueck and Krishna)	26
14. 3D Interferometric Lithography (Brueck)	30
2009 PUBLICATIONS	33
2010 PUBLICATIONS	35
2011 PUBLICATIONS	37
U. S. PATENT APPLICATIONS	39

Abstract

Research performed at the University of New Mexico under the AFOSR-supported optoelectronics Research Center is reported. This includes work on: high temperature nanoparticle phosphors, optomechanical oscillators, GaN nanoepitaxial growth and devices, dual-wavelength IR lasers for THz generation, CVD diamond and VECSEL integration, plasmonic detectors and focal plane arrays, and 3D interferometric lithography.

Introduction

The AFOSR-supported Optoelectronics Research Center at the Center for High Technology Materials at the University of New Mexico has continued to progress across a number of important areas as detailed in this report, covering the period April 1, 2011 to November 30, 2011. Research in materials, fabrication and devices is reported. While the detailed reports cover this limited period the publications list includes all publications for the full period of the grant: April 1, 2009 to November 30, 2011.

1. ZnSe:Mn/ZnS High Temperature Nanophosphors with Very High Quantum Efficiency for White LEDs (Osinski)

Efficient single-chip white LEDs are desirable in future lighting applications for optimal color rendering from the point of view of both human perception and energy efficiency. Single-chip white LEDs based on blue InGaN/GaN emitters are very attractive for general lighting because of their low cost and high luminescence efficiency. Most commercially available single-chip white LEDs are manufactured by combining a blue InGaN/GaN LED chip with a yellow phosphor, typically yttrium aluminum garnet (YAG) doped with cerium. White LEDs with the yellow phosphor emit an intense bluish white light, dominated by blue emission from the InGaN/GaN chip [1]. While many organic materials have been investigated for application as phosphors to improve the color rendering index of white LEDs, still their resulting emission is bluish white [2].

Our choice of Mn-doped ZnSe nanocrystals (NCs) is driven by their cadmium-free composition, bright emission well above room temperature [3,4], and their peak excitation in the violet – blue region. Quantum efficiency as high as 70% has recently been reported for Mn-doped ZnSe colloidal NCs [3]. Using colloidal synthesis, ZnSe:Mn/ZnS NCs were synthesized, emitting at the 497 nm peak and the Mn related 587 nm peak. These NCs were shelled with ZnS to provide additional isolation of the ZnSe:Mn NC core.

The synthesis for our ZnSe:Mn/ZnS NCs was adapted from Acharya *et al.* with significant modifications [5]. The ratio of Mn to Zn precursors, the large excess of Se at the beginning of synthesis, and the addition of S to the shell account for the significant modifications to the procedure that have resulted in this novel nanophosphor with record high QE.

In a typical synthesis, the Se precursor is prepared by adding 123 mg of selenourea to 10 mL of oleylamine in a three-neck flask. The solution is heated and stirred under argon until the selenou-

rea is completely dissolved, then it is allowed to cool. The core Zn precursor is prepared by adding 63 mg of zinc stearate (ZnSt_2) and 5 mL of octadecene (ODE) to a three-neck flask. The flask is then heated to 260 °C under argon; once the temperature is stabilized at 260 °C, all of the Se precursor is injected into the flask. The flask is then cooled to 240 °C. The Mn dopant is prepared by adding 6.3 mg of manganese stearate (MnSt_2) to 0.5 mL of ODE. The mixture is injected into the flask at 240 °C, the temperature is maintained until the dopant emission appears, and then the flask is heated to 260 °C.

The shell Zn precursor is prepared by adding 0.63 g of ZnSt_2 to 0.28 g of stearic acid (SA) and 10 mL of ODE to a three-neck flask. The ZnSt_2 /SA/ODE solution is then heated and stirred under argon for injection. To begin, 0.96 mL of the ZnSt_2 /SA/ODE solution is injected into the flask at 260 °C, and after 10 min another 0.96 mL is injected into the flask. The remainder of the shell is grown by progressively increasing injections of the ZnSt_2 /SA/ODE solution into the flask. The injection temperature for the flask is 260 °C, and after each injection the temperature is rapidly lowered to 240 °C. The four subsequent injections have the volumes of 1.33 mL, 1.69 mL, 2.25 mL, and 2.81 mL, respectively.

The shell S precursor is prepared by adding 15 mg of powder S to 1.5 mL of ODE, which is then injected into the flask at 260 °C. The flask is cooled to 240 °C for 15 minutes, then cooled to room temperature. The resulting NCs are washed by centrifugation using acetone, until a transparent supernatant is obtained. The supernatant is then discarded, while the NC precipitate is collected using toluene and stored in a brown glass bottle.

Photoluminescence (PL) and quantum efficiency (QE) were measured using a Horiba Jobin Yvon Fluorolog-3 spectrofluorometer, using Spectrosil® quartz cuvettes. ZnSe:Mn/ZnS NCs have two emission peaks: a shorter wavelength emission peak at 497 nm, and a longer wavelength emission peak at 587 nm. The 497 nm peak is excited by 453 nm light and has a shoulder at 525 nm, while the 587 nm peak is excited by 418 nm light, as shown in Fig. 1.

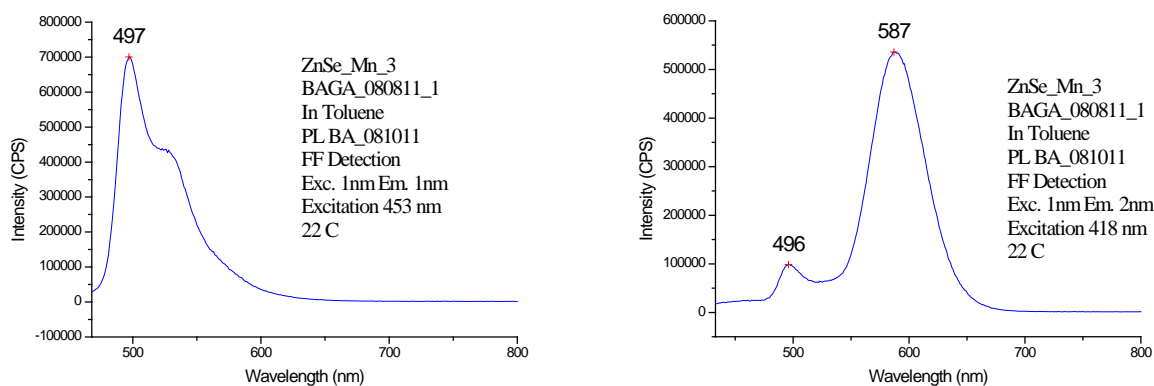


Fig. 1. PL spectra of ZnSe:Mn/ZnS/ZnSeS NCs in toluene, excited by 453-nm light (left) and by 418-nm light (right).

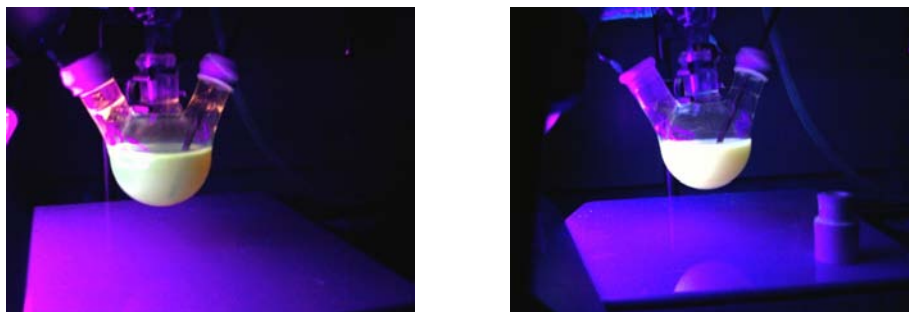


Fig. 2. PL emission from ZnSe:Mn/ZnS NCs during the synthesis at 240 °C (left) and after cooling down to room temperature (right).

QE measurements of ZnSe:Mn/ZnS NCs were performed using the Fluorolog-3 integrating sphere attachment and a liquid sample holder. Results from QE measurements At the 497 nm emission with 453 nm excitation, the measured QE was as high as 91%. At the 587 nm emission with 418 nm excitation, the QE was 39%.

Fig. 2 illustrates the high temperature emission from ZnSe:Mn/ZnS NCs, as observed during the synthesis. This is in contrast to CdSe/ZnS NCs, whose emission drops sharply with increasing temperature, and practically disappears above 60 °C. High PL efficiency at elevated temperatures makes the ZnSe:Mn/ZnS NCs particularly attractive for applications as nanophosphors in high-power white LEDs.

References

- J. K. Sheu, S. J. Chang, C. H. Kuo, Y. K. Su, L. W. Wu, Y. C. Lin, W. C. Lai, J. M. Tsai, G. C. Chi, and R. K. Wu, “White-light emission from near UV InGaN-GaN LED chip precoated with blue/green/red phosphors”, *Photon. Technol. Lett.* **15** (#1), pp. 18-20 (2003).
- F. Hide, P. Kozodoy, S. P. Denbaars, and A. J. Heeger, “White light from InGaN/conjugated polymer hybrid light-emitting diodes”, *Appl. Phys. Lett.* **70** (#20), pp. 2664-2666 (1997).
- N. Pradhan, D. Goorskey, J. Thessing, and X. Peng, “An alternative of CdSe nanocrystal emitters: Pure and tunable impurity emissions in ZnSe nanocrystals,” *J. Am. Chem. Soc.* **127**, pp. 17586-17587 (2005).
- N. Pradhan and X. Peng, “Efficient and color-tunable Mn-doped ZnSe nanocrystal emitters: Control of optical performance via greener synthetic chemistry”, *J. Am. Chem. Soc.* **129**, pp. 3339–3347 (2007).
- S. Acharya, D. D. Sarma, N. R. Jana, and N. Pradhan, “An alternate route to high-quality ZnSe and Mn-doped ZnSe nanocrystals,” *J. Phys. Chem. Lett.* **1**, pp. 485-488 (2010).

2. Harmonic RF frequency generation in optomechanical oscillator (OMOs) (Hossein-Zadeh)

We have finalized our experimental and theoretical study on harmonic generation in optomechanical oscillators. We now understand the relation between optical detuning, input power and the harmonic components in the power spectrum of the harmonic components. We have measured the detected power spectrum as a function of relative detuning Δ_L ($= \Delta/\delta_L$, $\Delta = \nu_{\text{laser}} - \nu_0$, ν_0 is the optical resonance and is δ_L the loaded optical bandwidth) and input power (P_{in}) values. The time domain coupled differential equations approach is in relatively good agreement with experimental outcomes for both low-power and high-power regime. However using this approach for each data point the equations should be solved separately. To simplify this process we have developed a relatively simple method based on the resonant optical transfer function (that we call TFM). TFM works very well for $P_{\text{in}} < 3 P_{\text{th}}$ and $f_{\text{OMO}} < \delta_L$. This is the preferred regime for OMO operation with reasonable phase-noise and minimal harmonic components (P_{th} is the threshold power and f_{OMO} is the mechanical oscillation frequency). Fig. 1(a) shows the typical RF spectrum of the OMO output power. Fig. 1(b) shows the measured harmonic components plotted against relative detuning for $P_{\text{in}} = 5.4 P_{\text{th}}$. As expected in the high power regime for large detuning the second and eventually the third harmonic become larger than the fundamental oscillation frequency. Fig. 1(c) shows the measured harmonic components plotted against relative detuning for $P_{\text{in}} = 1.8 P_{\text{th}}$. The solid lines are the theoretical prediction using our transfer function method (TFM). Soon we will submit a detailed report of our study to a peer-reviewed journal.

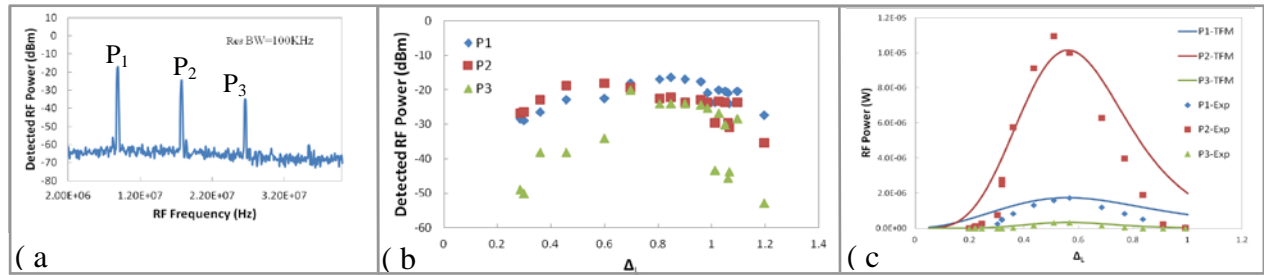


Fig. 1. (a) RF spectrum of the OMO output power for a typical silica microtoroid. P_1 , P_2 and P_3 are the fundamental, 2nd and 3rd harmonic components. (b) Experimentally measured harmonic components plotted against relative detuning (Δ_L = wavelength detuning/loaded linewidth) for $P_{\text{in}} = 5.4 P_{\text{th}}$. (c) Measured harmonic components plotted against Δ_L for $P_{\text{in}} \sim 1.8 P_{\text{th}}$. The solid lines are the theoretical prediction using the transfer function method (TFM) that we have developed.

Note: the final stage of these measurements has been done using the new RF spectrum analyzer that was purchased toward the end of the program (with permission from AFOSR). This analyzer has significantly improved the accuracy of our measurements and as a result the good agreement with theoretical predictions.

3. Optical control of microwave networks using bulk effects (Hossein-Zadeh)

We have studied and developed new configurations for optical control of microwave resonators based on bulk optical interaction. Almost all previous methods have focused on surface effects using laser wavelengths around 800 nm and the co-planar microwave structures. We fabricated a side-coupled microwave ring resonator on a silicon substrate for our study. The substrate thickness is 500 micron and the ground plane and the resonator-transmission line structure are created using RF sputtering of copper and photolithography. We created holes at different locations on the copper ring to test the effect of bulk illumination on regions with various distributions and strengths of microwave electric field. The collimated beam from a 1064 nm laser was used as the optical control beam. Based on the experimental values of silicon absorption the effective interaction length for 1064 nm photons is about 1 micron that corresponds to one round trip through the substrate. Note that the copper ground plane acts as a mirror at optical frequencies. Fig. 1(a) is a photograph of two samples under test. Fig 1(b) and 1(c) show the schematic diagram of the side-coupled ring as well as calculated electric field distribution in the middle of substrate at the fundamental resonant frequency. Fig. 1(d) shows the configuration used for vertical illumination of the sample.

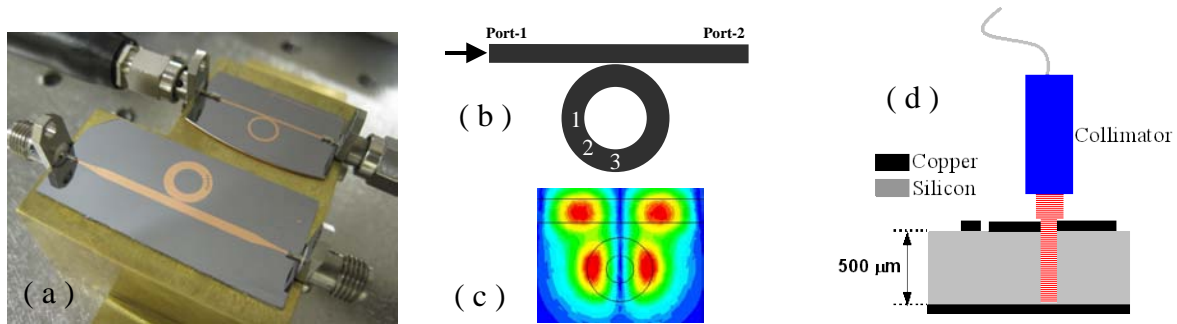


Fig. 1. (a) Photograph of the side coupled microwave ring resonator fabricated on a silicon substrate. (b) Schematic diagram of the side-coupled ring resonator and the locations where laser power has been focused on (in each case a hole is created on the copper to allow optical transmission). (c) Simulated electric field distribution in the middle of substrate at the fundamental resonant frequency of the microring resonator. (d) Vertical illumination of the sample by a collimated laser beam.

Fig. 2. shows the experimental results obtained with one of the rings that has been optically interrogated through a hole in location #2. The responses of the first and second resonant modes are monitored.

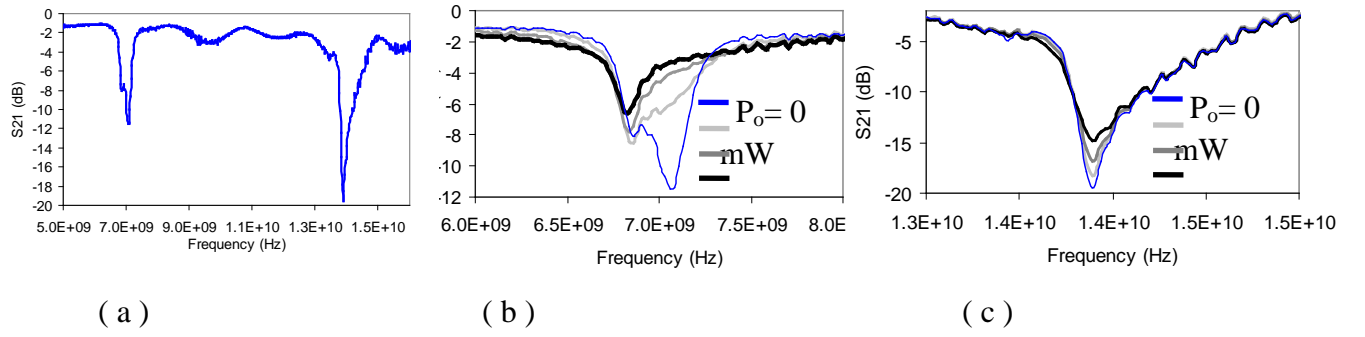


Fig. 2. (a) The spectrum of the transmitted RF power (S_{21}) through microstripline side-coupled to the RF ring resonator (showing the first and second resonant frequencies). (b) Transmission spectrum around the first resonance at different optical power levels. (c) Transmission spectrum around the second resonance at different optical power levels. Here the collimated laser beam (1064 nm) is placed on the spot #2 (see Fig. 1(c)).

The experimental results show that moving to longer wavelengths and using the bulk optical effect not only creates new possibilities for optically controlled microwave circuits but also may reduce the amount of optical power needed for controlling the microwave transfer function. The results of this study and design will be sent for publication soon.

4. Developing waveguides for on-chip integration of high-Q silica microtoroids (Hossein-Zadeh)

We have continued our effort on fabrication of polymer waveguide that is phase matched to a high-Q silica microtoroid. Using the fabrication facilities at Center for Integrated Nanotechnologies (CINT), we have been able to fabricate PMMA waveguides on CYTOP coated ITO substrate. Based on the waveguide dimension and numerical calculation this waveguide has an effective index very close to the silica fiber-tapers that are currently used to couple to microtoroids.

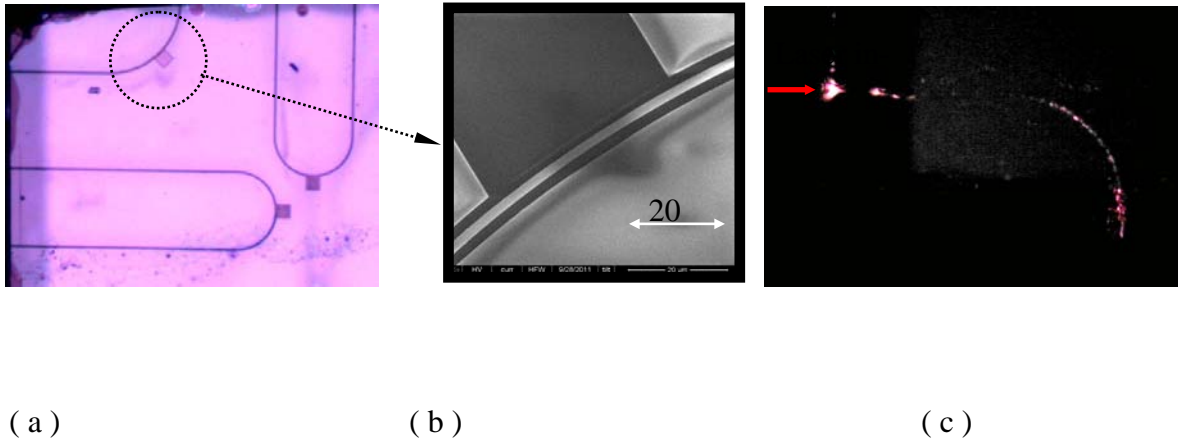


Fig. 1. (a) Top-view micrograph of the PMMA waveguides fabricated on a transparent substrate. (b) SEM image of the PMMA waveguide. (c) Top-view micrograph of red laser propagation through one of the waveguides.

5. Hybrid optomechanical resonator (Hossein-Zadeh)

Using CINT facilities we have been able to complete the fabrication process for a silica-Si₃N₄ optomechanical resonator. The results proved that the proposed fabrication process is feasible and can be used for a variety of hybrid high-Q optical microcavities. We have also simulated the mechanical behavior of these structures and calculated the resonant frequencies and effective masses associated with each mode. A provisional patent has been disclosed for the fabrication methods of hybrid microresonators.

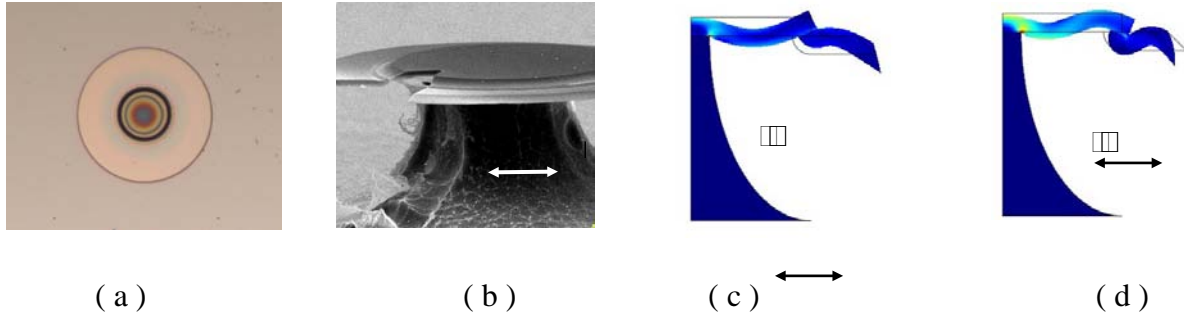


Fig. 1. (a) Top-view micrograph of a hybrid silica- Si₃N₄ before etching the silicon substrate. (b) SEM image of hybrid silica- Si₃N₄ microdisk on to of a silicon pillar (after XeF₂ etching). Focused-Ion-Beam (FIB) is used to cut a small section of the Microdisk to observe and study the interface between thermally grown silica and the Si₃N₄ microdisk. (c) and (d) Simulated mechanical displacement of the hybrid microdisk resonator for the third ($f_{RF} = 48$ MHz) and sixth ($f_{RF} = 134$ MHz) mechanical modes of the structure.

6. GaN Growth and Devices (Hersee)

During the last year this project has focused on exploring the novel capabilities of templated, non-planar GaN growth to better understand the underlying growth mechanism and to determine the full potential of this revolutionary process.

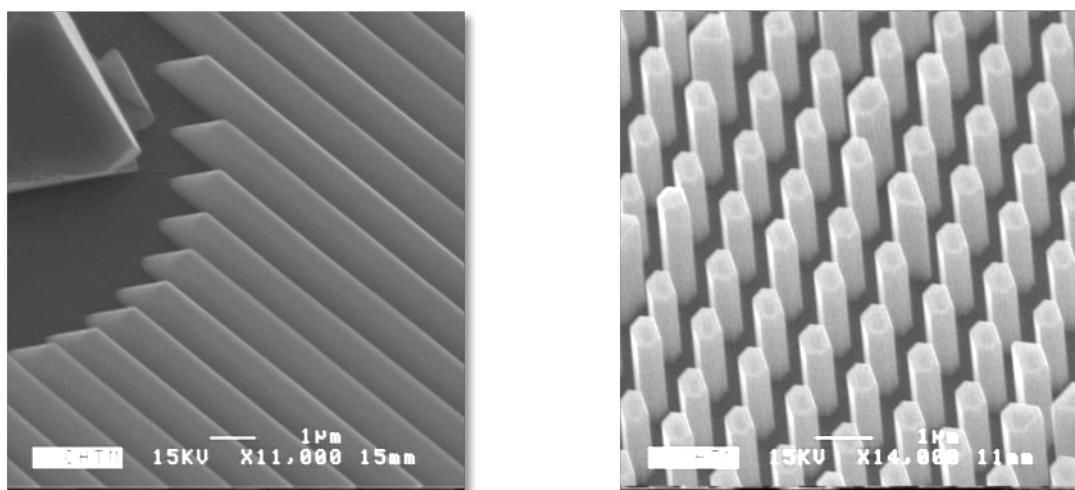


Figure 1: Nonplanar GaN Structures. Nanowalls (left) and nanowires (right)

The basic templated growth process has been described in previous reports¹. Briefly, this MOCVD (metalorganic chemical vapor deposition) approach uses standard TMGa and NH₃ precursors and requires no additional catalysts. When optimized this process grows massive arrays of uniform GaN nonplanar objects. For example, Fig. 1 shows an array of nanowalls (left) and an array of nanowires (right) grown by this approach. The sidewall facets of these objects are atomically smooth $\{1\bar{1}00\}$ facets and as shown in previous reports we can grow high quality III-N on these sidewalls. The direction perpendicular to these facets is non-polar in GaN, which means that unlike normal GaN grown on c-oriented sapphire substrates, the GaN grown on these sidewall facets has NO built-in electric fields. The absence of built-in electric field is important for many devices such as LEDs or transistors, and these sidewalls thus represent a rich opportunity for developing a new family of nonplanar and non-polar GaN devices.

The lateral shape of the nonplanar GaN objects (i.e., their cross-section) is controlled by the shape of the aperture in the growth template (aka growth mask). The vertical growth rate of these non-planar objects is, however, a complex function of their geometry and their pitch as described below.

There are 2 fluxes of nutrient that contribute to the growth of each non-planar object (Fig. 2). There is a flux (#7) from the gas phase falling directly on the non-planar object. There is a second flux that initially hits the growth mask (#1), where no growth takes place, and then either

evaporates (#2) from the mask surface or moves sideways (#3) to contribute to growth of an adjacent nonplanar object.

The amount of lateral growth flux will vary with the spacing of the nonplanar objects. When they are close together they compete for nutrient and the lateral growth flux per object is reduced.

SURFACE DIFFUSION

1. Growth nutrient arrives at sample surface
2. Evaporation
3. Nutrient within “capture radius” diffuses to nanowire
4. Evaporation
5. Surface diffusion and growth on sidewall
6. Growth at nanowire tip

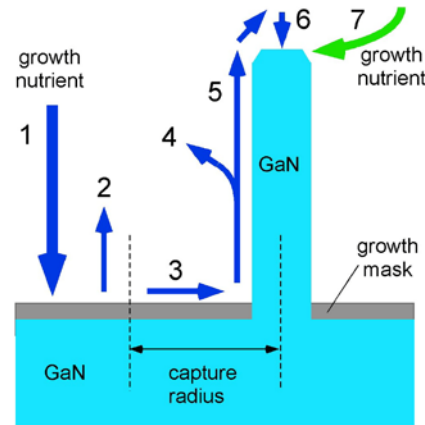


Fig. 2: Schematic of growth and diffusion processes.

GAS PHASE DIFFUSION

7. Growth from gas phase to nonplanar GaN object

It is useful to consider a “capture radius” extending around the object. Growth nutrient that lands within the capture distance will contribute to the growing structure. For example, if we assume 5 micron capture distance and a 10 micron diameter object - then everything within a 20 micron diameter (centered on this hole) will be captured by this growing object ($10+5+5$). If we assume a 5 micron capture distance hole with a 1 micron diameter object, then everything within an 11 micron diameter ($1+5+5$) will be captured by the structure. (Of course, when two nonplanar objects are spaced at less than the capture radius, then the two objects will compete for the growth nutrient.) The volume of the nonplanar object should therefore be proportional to this total cap-

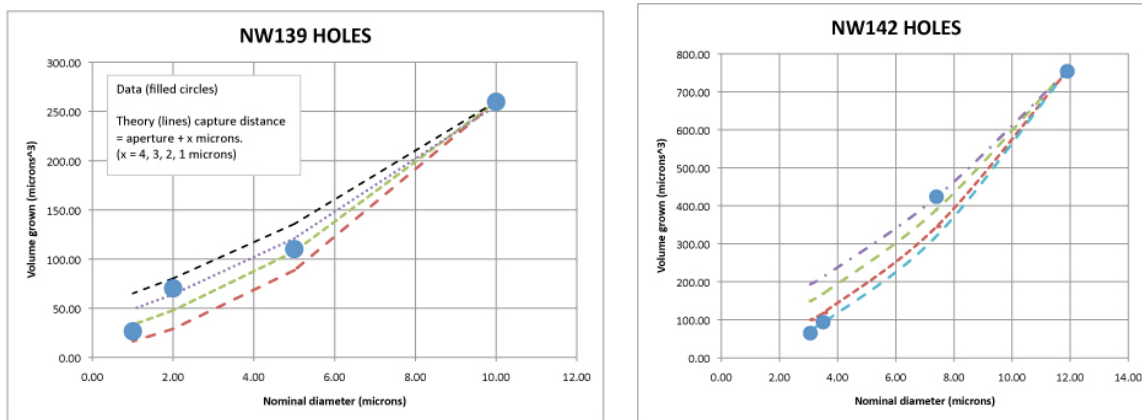


Figure 3: Left side shows data and theory for NW 139 and the plotted theory lines are for the following capture distances: 4, 3, 2, 1 microns. Right side shows data and theory for NW 142 and the plotted theory lines are for the following capture distances: 3, 2, 1, 0.5 microns.

ture area and this was tested against SEM data for 2 growths NW 139 and NW 142. Fig. 3 plots the variation of the object volume as a function of its diameter, for 4 different capture radius values. Based on this data the capture radius is approximately 1.5 microns.

Thus when the object has a small cross-section, eg. < 1 micron diameter, the contribution of the

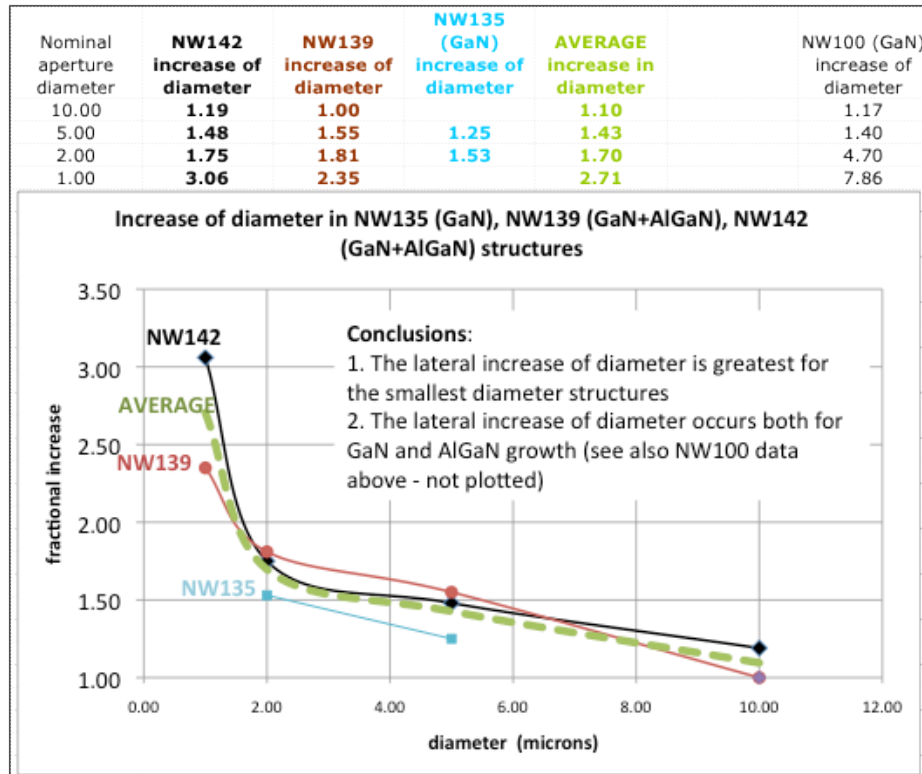


Fig. 4: Increase in object diameter relative to the mask aperture diameter, as a function of the object diameter.

lateral flux will dominate and there will be a larger inward flowing (lateral) growth rate towards the central structure. The maximum lateral flow will occur for the smallest structures and will be greatest at the start of these structures. This might explain why the smallest structures are observed to show the biggest increase in diameter relative to the mask aperture size. In the case of the larger diameter structures the sideways flow will make a relatively small growth contribution and these structures are observed to maintain approximately the same diameter as the aperture in the growth mask. This behavior is clearly demonstrated by Fig. 4, which plots the increase in object diameter relative to the

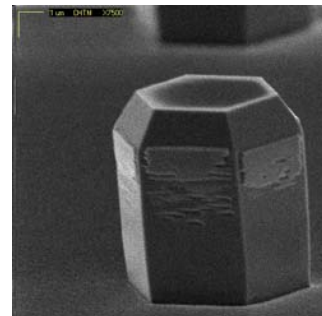


Figure 5: Non-uniform AlGaN growth on the sidewalls of a GaN nanowire core

mask aperture diameter, as a function of the object diameter.

The basic growth of these nonplanar GaN objects is now well understood. However, more work is needed to understand some of the more subtle growth behavior. For example, when AlGaIn is deposited on the sidewalls of a GaN nanowire, we sometimes observe a non-uniform coverage of the sidewall as in Fig. 5.

The work described above is being prepared for publication. Other publications and a patent resulting from this project are listed in the publications and patents section of the report.

1 S. D. Hersee, X. Sun, X. Wang, "The Controlled Growth of GaN Nanowires", Nano Lett., 6, 1808 – 1811 (2006).

7. Dual Wavelength QD Sources for THz Generation (Lester)

Applications for THz radiation are diverse, encompassing homeland security, computing and communications technologies, medical and pharmaceutical fields as well as basic material science¹⁻⁶. THz waves can be generated by coherently interfering two optical modes, which are generated by two separate single-mode lasers. The light is then absorbed in an ultrafast photoconductive semiconductor⁷⁻⁹. An alternative approach simultaneously generates dual wavelength emission from a single laser cavity. This approach has the advantage of being free of optical alignment issues since there is no need to align two laser beams—a critical requirement for photomixing efficiency. Typically, dual wavelength emission from quantum well (QW) lasers requires two separate gratings to be incorporated into the device. Furthermore, the tunability associated with these devices is limited by the bandwidth of the QW gain profile.¹⁰ By contrast, quantum dot (QD) lasers offer a more flexible platform to generate tunable dual-wavelength emission. Simultaneous ground state (GS) and excited state (ES) operation with multi-mode emission has been previously observed in QD lasers and was attributed to the incomplete clamping of the ES carrier population at the GS threshold, in contrast to the complete clamping of the threshold carrier density associated with QW lasers.¹⁴ Due to the relatively low density of states inherent to QDs and consequent unique carrier dynamics, dual-wavelength emission consisting of a single distributed feedback (DFB) mode and a single Fabry-Perot mode, both originating from the same inhomogeneously broadened QD transition can be realized. This phenomena of accessing different carrier populations in an inhomogeneously broadened system is not likely in a QW active region because of the contrasting carrier dynamics associated with a homogeneously broadened continuous density of states.¹¹ The wide gain bandwidth characteristic of QD nanostructures enables a relatively large frequency difference between the two modes.

Recently, a novel dual-mode emission was demonstrated in a two-section QD laser where one mode was coupled to a Bragg grating and the other to the Fabry-Perot (FP) cavity.¹² It was shown that the relative spectral intensities between the QD GS and ES modes could be equalized, resulting in a simultaneous dual-mode emission with an 8-THz frequency difference. Following the same concept with a similar device, our work focused on the generation of dual-modes from the QD ES only with one peak being coupled to the grating and the other to the FP cavity. By appropriately combining asymmetric pumping with controlled optical feedback, it is shown that the observed mode frequency difference can be tuned from 1.3-THz to 3.6-THz over a wide temperature range. These results are enabled through the unique nature of the QD media via the ES inhomogeneous linewidth and are also coupled with the effects of using an external stabilization mechanism. The technical approach described in this paper addresses the need for compact size and low fabrication cost, which is significant for the development of future THz optoelectronic sources.

In order to increase the laser's stability as well as to manipulate the different FP cavity modes, an optical fiber-based feedback loop was implemented in the experimental setup. The feedback loop

to the laser consisted of a four-port polarization-maintaining (PM) 50/50 fiber coupler. The DFB laser output light was injected into port 1, and The optical feedback was then created using a high-reflectivity coated fiber connected to port 2. The applied external feedback level was controlled via a fiber-based variable attenuator at port 4. The impact of the external optical feedback on the laser spectrum was analyzed with a resolution of 10 pm. The distance between the laser and the external reflector is estimated to be a few meters, which corresponds to an external roundtrip time of about 10–30 ns (long external cavity condition).¹³ The amount of injected optical feedback into the laser, Γ , is defined as the ratio between the reflected power and the emitted power. Figure 1(a) shows the optical spectra recorded under asymmetric pumping at the lowest temperature (5°C) and for a total pump current of 115-mA (66.5-mA/48.5-mA). In Fig. 1(a), the red spectrum corresponds to the solitary laser while the blue one is obtained for an optimum feedback level of $\Gamma=2\times 10^{-3}$. Results show that optimizing the applied external feedback conditions leads to the generation of an additional mode lasing at 1208.1-nm and related to the FP cavity, which is also located within the ES inhomogeneously broadened bandwidth.

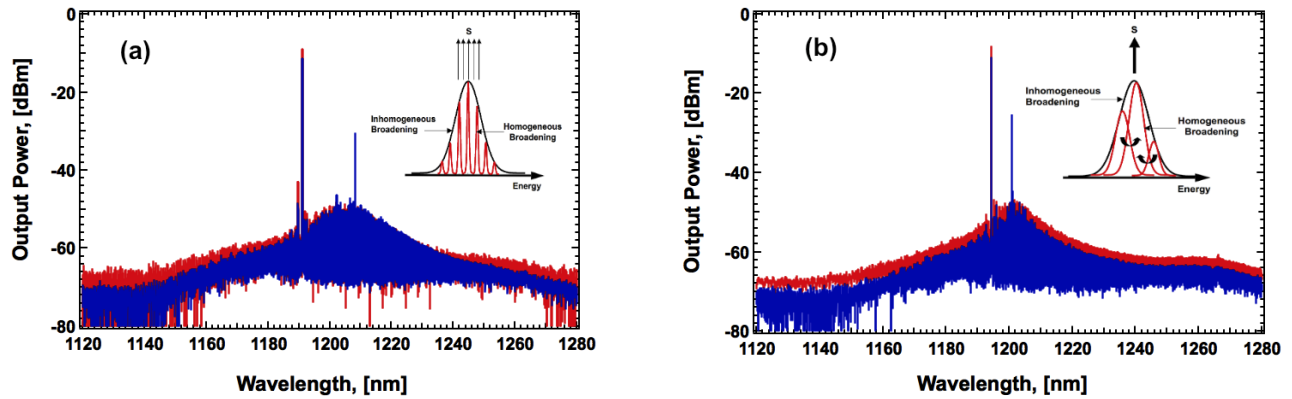


FIG. 1. Spectra under total asymmetric pump current for the solitary laser (red) and under controlled optical feedback (blue) at (a) 5°C and (b) 40°C.

Since the ES DFB peak remains robust and stable as a result of strong Bragg gratings, a dual-mode emission with 3.6-THz frequency difference is demonstrated. Figure 1(b) shows similar results for the highest temperature (40°C) but for a total pump current of 153-mA (86-mA/67-mA). Although the total pump current had to be increased to compensate for temperature-related effects, it is important to note that the ratio of current in each section was kept constant at around 1.3 throughout the entire experiment. Under the highest achievable optical feedback level of $\Gamma=4\times 10^{-3}$, a separate FP-generated peak excites at 1200.1 nm, which is 8-nm away from the grating coupled ES mode. This configuration leads to dual-mode emission with a 1.3-THz frequency difference. In order to summarize the experimental findings, the variations of the frequency difference (left axis) over temperature as well as the corresponding SMSR (right axis) are illustrated in Fig. 2. In this figure, each point is measured for the configuration that yielded the optimum

optical feedback condition. Solid lines in Fig. 2 are used as a guide for the eye. Based on these results it can be deduced that the frequency difference is progressively tuned closer to the gain peak from 3.6-THz all the way down to 1.3-THz when the temperature is decreased successively from 40°C to 5°C. The corresponding SMSR ranged from 10-dB to 20-dB meaning that in all

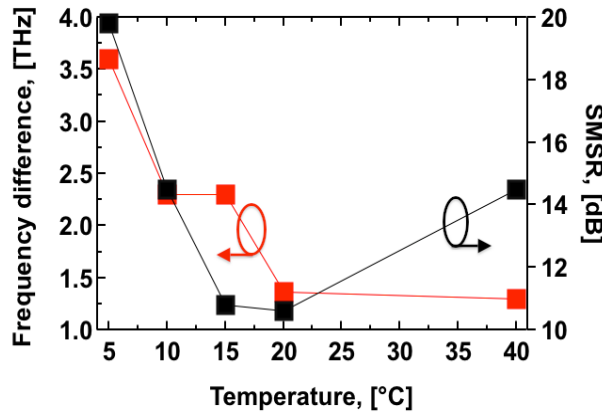


FIG. 2. Measured THz frequency difference (red squares) and Side Mode Suppression Ratio (black squares) as a function of the temperature under the best optical feedback

cases studied here, the two peak powers could not be equalized due to the limited optical feedback amplitude as well as the loss induced by the fiber-based feedback setup. The optical feedback is known to induce variations in stimulated emission, which are provoked by the beating of the photons with the delayed field. Consequently, the carrier fluctuations related to the cavity photons can deplete carriers from both resonant QD states inside the homogeneous broadening as well as non-resonant states outside. The small decrease in the DFB peak power under optical feedback can be explained by the carrier depletion of the resonant QD states, which are transferred to another dot population. The DFB and FP cavity mode

shifts do not exceed 0.10-nm/°C and 0.16-nm/°C respectively; therefore, these variations alone cannot explain the change in the observed frequency difference with temperature. Another important point to take into account is the temperature and injected current level dependence of the homogeneous broadening.¹⁴ At low temperature, dots with different energies remain spatially isolated from each other (see inset of Fig. 1(a)) while they get spatially and energetically connected to each other at higher temperatures (inset of Fig. 2(b)). The homogeneous linewidth also increases with increasing current injection.¹⁵ The combination of these three effects can explain the progressive shift with temperature of the resonant mode towards the ES gain peak. Although simultaneous GS and ES with multi-mode emissions have been previously observed in QD material when increasing the bias current well above the threshold,^{11,16} the results of our work are the first to demonstrate dual-modes operating in the ES. To conclude, dual-mode lasing within the ES inhomogeneous broadening can be manipulated via a suitable combination of asymmetric pumping and external optical feedback in a two-section QD laser. This technique could enable THz frequency generation ranging from 1.3-THz to 3.6-THz. Generation of the dual-mode output is mainly attributed to the unique nature of the QD media through the ES inhomogeneous linewidth manipulation using the external control technique.

¹M. Koch, Terahertz Frequency Detection and Identification of Materials and Objects, R. E. Miles, X. -C. Zhang, H. Eisele, A. Krotkus, eds. (Springer, New York, 2007).

²P. H. Siegel, IEEE Trans. Microw. Theory Tech., **52**, 2438–2447, (2004).

- ³P. F. Taday, *Phil. Trans. Royal Soc. London*, **362**, 351–364, (2004).
- ⁴S. Wang, B. Ferguson, D. Abbott, and X.-C. Zhang, *J. Biol. Phys.*, **29**, 247–256, (2003).
- ⁵M. Naftaly and R. E. Miles, *Proceedings of IEEE on T-Ray Imaging, Sensing, and Retection*, Institute of Electrical and Electronics Engineers, pp. 1658–1665, (2007).
- ⁶C. Baker, T. Lo, W. R. Tribe, B. E. Cole, M. R. Hogbin, and M. C. Kemp, *Proceedings of IEEE on T-Ray Imaging, Sensing, and Retection*, Institute of Electrical and Electronics Engineers, pp. 1559–1565, (2007).
- ⁷R. Mendis, C. Sydlo, J. Sigmund, M. Feiginov, P. Meissner, and H. L. Hartnagel, *Int. J. Infrared Millim. Waves*, **26**, 201–207, (2005).
- ⁸M. Tani, O. Morikawa, S. Matsuura, and M. Hangyo, *Semicond. Sci. Technol.*, **20**, S151–S163, (2005).
- ⁹M. Naftaly, M. R. Stone, A. Malcoci, R. E. Miles, and I. Camara Mayorga, *Electron. Lett.*, **41**, 128–129, (2005).
- ¹⁰S. D. Roh, T. S. Yeoh, R. B. Swint, A. E. Huber, C. Y. Woo, J. S. Hughes and J. J. Coleman, *IEEE Phot. Technol. Lett.*, **12**, pp. 1307-1309, (2000).
- ¹¹A. Markus, J. X. Chen, C. Paranthoen and A. Fiore, *Appl. Phys. Lett.* **82**, 1818-1820, (2003).
- ¹²N. A. Naderi, F. Grillot, A. Gin, and L. F. Lester, *Optics Express*, **18**, 27028-27035, (2011).
- ¹³D. M. Kane and K. A. Shore, *Unlocking dynamical diversity*, Wiley, 2005.
- ¹⁴F. Grillot, K. Veselinov, M. Gioannini, I. Montrosset, J. Even, R. Piron, E. Homeyer, S. Loua-liche, *IEEE J. of Quantum Electron.*, **45**, pp. 872-978, (2009).
- ¹⁵P. Borri, W. Langbein, S. Schneider, U. Woggon, R. L. Sellin, D. Ouyang and D. Bimberg, *IEEE J. Sel. Topics Quantum Electron.*, **8**, pp. 984-991, (2002).
- ¹⁶M. A. Cataluna, D. I. Nikitichev, S. Mikroulis, H. Simos, C. Simos, C. Mesaritakis, D. Syvridis, I. Krestnikov, D. Livshits, and E. U. Rafailov, *Optics Express*, **18**, pp. 12832-12838, (2010).

8. CVD diamond and VECSEL integration (Balakrishnan).

In this year a considerable amount of research was done into the growth, characterization and thermal analysis of the poly-crystalline layers on CVD diamond. We demonstrated the growth of polycrystalline GaAs thin-films on polycrystalline Chemical Vapor Deposition (CVD) diamond by Low-Temperature Molecular Beam Epitaxy (LT-MBE). The Low Temperature GaAs (LT-GaAs) layer is easily polished compared to the CVD diamond, and this process results in a reduction of RMS surface roughness from > 50 nm to < 5 nm. This makes the LT-GaAs on diamond layer an ideal wafer-bonding interface for high-power semiconductor devices. The samples were grown at $0.2 \mu\text{m/hr}$ with a substrate temperature of 250°C and a 1:8 III/V beam equivalent pressure ratio. The samples were analyzed by X-Ray powder-diffraction, atomic force microscopy for surface roughness and in-situ reflective high-energy electron diffraction (RHEED) during MBE growth. We also measured the thermal conductivity of the GaAs layer on CVD diamond using pump-probe time domain thermoreflectance.

Finally, we measured the thermal conductivity of the polycrystalline GaAs films with a pump-probe time domain thermoreflectance (TDTR) setup located at the Sandia National Labs. Details of the experimental setup and thermal analysis are discussed in detail elsewhere.

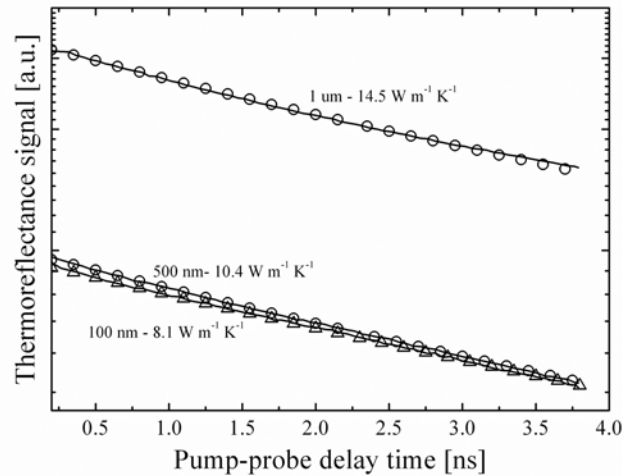


Fig. 1 Thermal conductivities of 1 μm , 500 nm, and 100 nm poly-GaAs films on CVD diamond as measured using pump-probe time domain thermoreflectance.

From the thermal measurements shown in fig. 1, the polycrystalline GaAs films show promise as an improved thermal interface material (TIM) for diamond heat sinks over traditionally used indium solders. Typical indium solder thermal interface materials have thicknesses on the order of several microns. Assuming a bulk value for the thermal conductivity of In ($81.8 \text{ W m}^{-1} \text{K}^{-1}$), the thermal resistance of a 10 mm TIM of In is $1.22 \times 10^{-7} \text{ m}^2 \text{K W}^{-1}$. Although the thermal conductivities of the polycrystalline GaAs films are less than that of bulk indium, the required film thickness is much lower than the typical thickness of In used as TIMs. For the 100

nm polycrystalline GaAs films measured in this study, the thermal resistance is $1.2 \times 10^{-8} \text{ m}^2 \text{ K W}^{-1}$, a thermal resistance that is a factor of 10 lower than a traditional In TIM.

9. Quantum dot VECSELs. (Balakrishnan)

Perhaps the most important innovation in developing world-record quantum dot lasers is the introduction of *single dot-layer per antinode resonant periodic gain designs*. We have developed a resonant periodic gain (RPG) structure with a single QD layer per standing wave antinode to effectively increase the distance between strained layers to improve the quality of the active region. We have already compared the performance of a VECSEL with 12 separate QD layers ("12x1" structure) to a more traditional design that uses 4 groups of 3 closely spaced QD layers ("4x3"). The experimental performance of the 12x1 device is superior to the 4x3 structure in terms of threshold pump power, differential efficiency, and maximum output power.

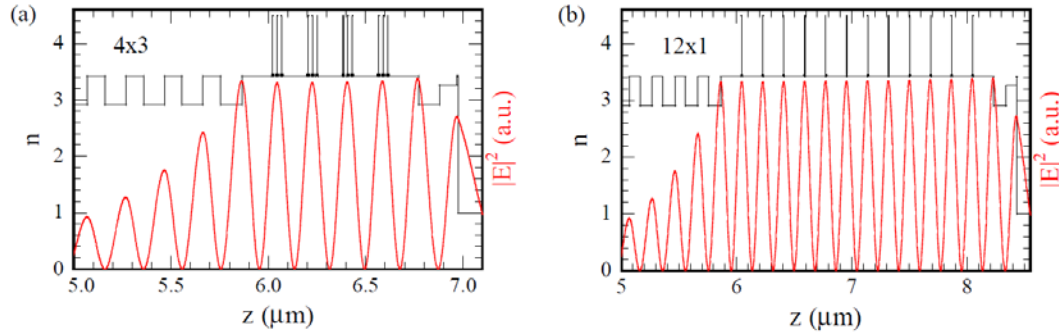


Fig. 2: Two different resonant periodic gain designs for InAs QD based VECSELs. The design on the left has three dot layers per antinode (4x3 design) of the E-field standing wave and the design on the right has a single dot layer per antinode (12x1 design).

The VECSEL structures were grown in a Vacuum-Generators V80 molecular beam epitaxy (MBE) reactor on 3 inch diameter GaAs substrates. After oxide desorption, the DBR consisting of 30 pairs of quarter-wave optical thickness AlAs and GaAs layers was grown. The InAs QDs were formed by depositing 1.68 monolayers of InAs inside 7 nm thick $\text{In}_{0.15}\text{Ga}_{0.85}\text{As}$ quantum wells grown at a substrate temperature of 480°C as determined by optical pyrometry. For the 4x3 structure, 3 QD layers are separated by 15 nm GaAs barriers, and repeated 4 times at adjacent standing wave antinodes, resulting in a total GaAs barrier/subcavity thickness of $0.9 \mu\text{m}$. In the case of the 12x1 RPG design, a single QD layer is placed at 12 consecutive antinodes, resulting in a subcavity thickness of almost $2.4 \mu\text{m}$. These designs are shown in Figure 2. While this should be beneficial due to a more complete absorption of incident pump light, it also results in larger pump non-uniformity across the QD layers. Both VECSEL structures are capped with one DBR pair consisting of AlAs and $\text{Al}_{0.3}\text{Ga}_{0.7}\text{As}$ (transparent to the 808 nm pump light) to both

prevent surface recombination and reduce lasing threshold. The optically pumped VECSELs were then compared for a variety of lasing studies and the results have been published in JSTQE and JVST B (included in publications list).

10. Plasmonic fluorophores (Jain)

Several novel plasmon-enhanced quantum dot (QD) light emitters were designed and analyzed theoretically in detail this year; in addition, several preliminary structures, starting with growth of spherical silica shells of nm thickness around CdSe QDs, have been fabricated during this year.

The proposed “plasmonic QD” light emitter consists of a semiconductor quantum dot surrounded by successive layers of insulating dielectric material (silica or a non-conductive polymer), which in turn are surrounded by ultrathin field-enhancing plasmonic noble metal shells (typically silver or gold). Simulations of the spatial distribution of the electric field enhancement factor in such a structure (under x-polarized plane wave illumination) – immersed in water -- are shown in the false color plot of Figure 1 for a silica-coated CdSe SQD (of 6 nm diameter) surrounded by a gold shell of 26 nm outer radius and 23 nm inner radius. It is clear from this figure that such a quantum dot is expected to experience an electric field enhancement (EFE) of > 8 (color coded as navy blue) over most of its volume, leading to enhancement of two-photon-absorption-induced fluorescence (TPAF) by factors exceeding 2400.

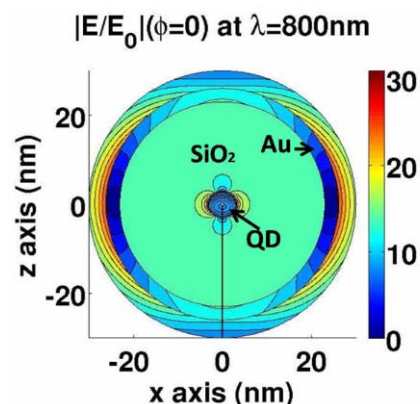


Fig. 1: EFE (electric field enhancement factors) for a 6nm QD with a silica shell of 23 nm radius and a 3nm outer gold shell.

Such light emitting nanoparticles can be fabricated by several methods. In one such method, colloidal semiconductor QDs with an octadecylamine (ODA) ligand, are mixed with tetraethyl orthosilicate (TEOS) -- a silica precursor -- and ammonia in cyclohexane to form a water-in-oil reverse microemulsion. The QD, TEOS and ammonia localize into reverse micelles where the ammonia hydrolyzes the TEOS to separate the silica and deposit it in the form of highly uniform and ultrathin silica layers on the QDs. Using this method we synthesized the particles seen in the TEM image in Figure 2. These will next be coated with ultrathin (2 - 3 nm thick) layers of gold to create the structure shown in Figure 1.

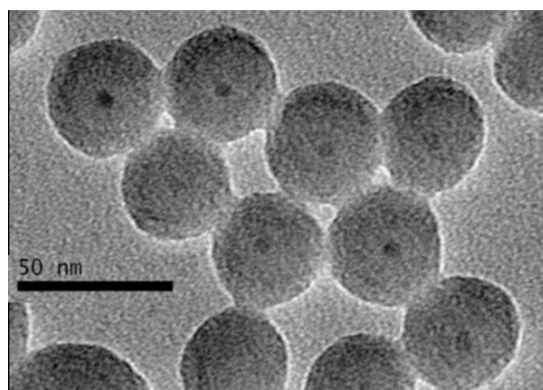


Fig. 2: TEM image of silica-coated QD using the method described in the text.

Multilayered structures with QD core with multiple alternating dielectric and noble metal layers or “shells” were analyzed and optimized, leading to designs with theoretical TPAF enhancements of 160,000 in the QD core. One such optimized structure consists of a 12 nm radius inner titania layer, a 6 nm thick inner Ag shell, an 80 nm thick outer titania layer, and an outer Ag shell

of 8 nm thickness; the field enhancement plots for such a structure in an aqueous environment are shown in Figs 3 and 4 [7, 8].

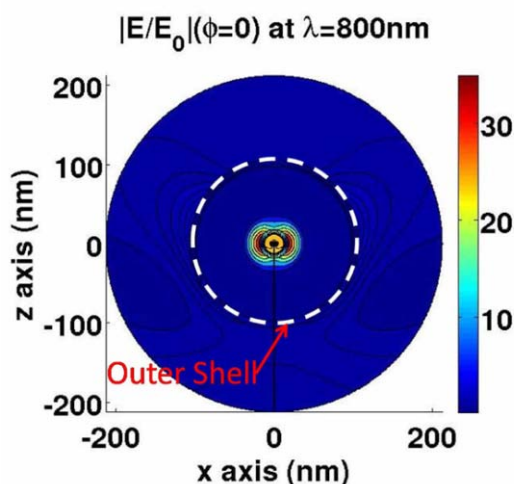


Fig. 3: EFE for a 12 nm radius inner titania layer, 6 nm thick inner Ag shell, 80 nm thick outer titania layer, and an outer Ag shell of 8 nm thickness, in water.

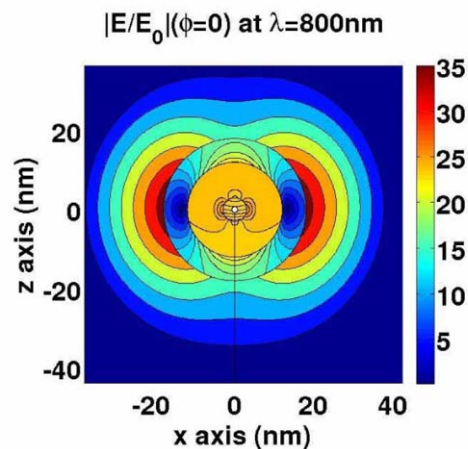


Fig. 4: The same as the previous figure zoomed in around the inner Ag layer.

We have also developed a TPAF imaging system for the characterization of various fluorophores via linear and non-linear excitation. Baseline experiments on uncoated SQDs (with no plasmonic enhancement) have been recently performed and reported in these structures [3, 4].

Once the mechanisms of enhanced light absorption and emission from plasmonic quantum dot structures are well-understood, we will also explore the design and fabrication of optimized composite structures for other advanced plasmonic devices, such as ultrahigh efficiency solar cells and brighter high-efficiency LEDs. For solar cell applications, the use of plasmon-enhanced light absorption seems superior to the use of roughened surfaces for increased light absorption (since roughened surfaces suffer the disadvantage of increased surface recombination). Note that this research effort is jointly supported by this grant and another AFOSR grant (PM: G. Pomrenke)

11. Plasmonic Tunnel Junctions (Jain):

We have demonstrated near-IR light emission from MIM tunnel junctions – in a research effort also supported jointly by this grant and another AFOSR grant (PM: Pomrenke) – from grating-coupled and randomly structured junctions [5, 6]. This research shows clear evidence of SPP (surface plasmon polariton) generation by tunneling electrons in carefully-designed MIM (metal-insulator-metal) structures, and has strong potential for the development of on-chip SPP generators for miniaturized plasmonic circuits.

12. Advanced Microstructured Fibers (Jain)

Fiber lasers have unique properties that are preferred in high power/energy output, such as good beam quality and compactness. Ultra-large mode area microstructured fibers are critical for such high power fibers lasers. A companion AFOSR DURIP grant, along with manpower support under this grant, has been used to build a state-of-the-art fiber fabrication facility that will be used in the near future for the fabrication of advanced microstructured fibers. Our primary near-term focus is on fabricating fibers that will lead to single-polarization, single-transverse-mode, robust, narrow-bandwidth kilowatt-level fiber lasers that will be easily manufacturable and easy to incorporate in various beam combining laser systems, while meeting the following specifications: (1) single-mode outputs with M^2 better than 1.05, (2) single-mode polarization with polarization extinction ratio better than 20 dB, (3) output linewidths less than 5 GHz to minimize SBS problems during high-power scaling, and (4) electrical-to-optical conversion efficiencies of better than 25% (with a long-term goal of extending these efficiencies to 40%).

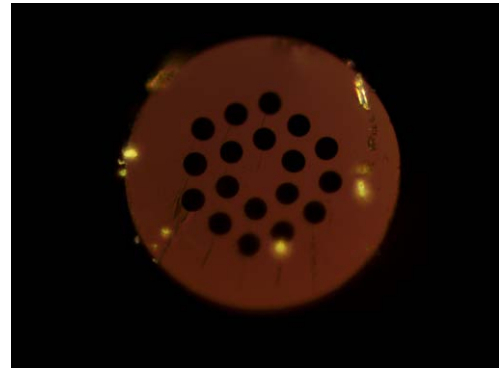


Fig. 1: Microscopic image of fabricated 125 micron diameter holey fiber

We have successfully demonstrated drawing of fibers with diameters in the range of 50-225 microns -- of several hundred meters length -- from conventional silica fiber preforms, and have designed and fabricated several microstructured fiber preforms for endlessly single mode fibers. Several experiments have been performed to study heat propagation within the silica preform and the effects of internal pressurization on the preform's internal structure. We have also designed and fabricated a custom water-cooled fixture and an "overpressure system" that is used to create a controlled overpressure inside the "holey" preform (with an accuracy of 2-3kPa) and thereby control the final geometry of the drawn microstructured fiber. We are in the process of fine-tuning the pressure control system to be stable to 1kPa, which will enable precise control of the internal fiber geometry, as required for reproducible fabrication of complex microstructured fibers.

We have successfully fabricated microstructured fibers a few times during the last year using a capillary stack-based hexagonal hole pattern (Fig. 1 illustrates one such 125-micron diameter fiber fabricated in our fiber fab facility this year). We are in the process of optimizing the pressure and temperature control parameters to vary the size of these holes. After completion of this study, we plan to attempt fabrication of a rectangular hole lattice in the near future, followed by fabrication of a set of capillaries of varying IDs to obtain a unidirectional linear effective index tilt in the microstructured fiber to demonstrate an extremely low-loss VLMA fiber; the proposed VLMA fiber design will represent a major advance in the design of high power fiber lasers, an area of great interest to – and of a planned collaboration with – researchers at AFRL, Kirtland AFB.

13. Plasmonic Infrared Detectors and Focal Plane Arrays (Brueck and Krishna)

Infrared imaging (3- to 14- μm) is critical to many defense and civilian missions. The infrared has long been a mainstay for defense sensing and warning including defeating camouflage,¹ remote identification of chemical and biological compounds,² and anomaly detection.³ Civilian applications include fire detection and monitoring, perimeter monitoring of chemical facilities, and medical applications.⁴ Infrared imaging has improved from mechanically scanned single pixel detectors, to linear arrays and to today's high pixel count (to 16 Mpixel and higher) focal plane arrays. However, the photon detector technology in the main relies on InSb (MWIR, 3-5 μm) and HgCdTe systems (LWIR, 8-12 μm) that have been improved upon incrementally for at least 50 years – technologies that are widely available to friend and foe alike.⁵ Important directions in infrared sensor technology are: high operation temperature (HOT), multi/hyperspectral sensing and polarimetry. This project addresses all of these issues by adding plasmonic functionality to III-V based focal plane array technologies including quantum dots (QD) and strained layer superlattices. QD detectors have demonstrated very low dark current but suffer low quantum efficiency due to a low fill factor and weak absorption⁶. The proposed approach will enhance the quantum efficiency (QE) for QD-based devices close to 100% (or alternatively allow reduction of the dark current for superlattice detectors by reducing the active volume without sacrificing QE) addressing the HOT requirement while allowing the use of a III-V based material system with significant manufacturability advantages. The plasmonic structure can be modified at each pixel to encode both spectral and polarization selectivity into the focal plane array; a dramatic simplification compared to current, *ad hoc* filter-based approaches, opening a new paradigm in bio-inspired spectral-polarimetric sensing. The combination is a big enough step to claim a next generation in infrared imaging technology and to shift the balance back to US technological advantage.

Plasmonic Coupling to Infrared Photon Detectors Recently, the optical properties of a thin metal film perforated by 2-dimensional (2D) hole arrays, a metal photonic crystal (MPC), and the role of surface plasma waves (SPWs) in the extraordinary optical transmission of this MPC have been studied extensively.⁷ The SPW is bound to the metal/dielectric interface with an evanescent field that decays exponentially away from the interface. Resonances are observed when a wavevector of the array provides phase-matching between the incident photon and SPWs at either of the metal/dielectric interfaces. We have demonstrated a significant, 30 \times , enhancement in the response of InAs:GaAs dots in a well (DWELL) photodetectors by adding a plasmonic structure.⁸ Fig. 1 shows the structure and the responsivity enhancement.

This result was for a large, 400 μm diameter, pixel. In a focal plane the typical pixel dimension is $\sim 25 \mu\text{m}$. There remain significant questions toward optimizing the final structure. What is the impact of the QD absorption on the plasmon propagation? How high a quantum efficiency can be achieved and for what pixel dimension? What is the impact of the heavily-doped contact layer

between the metal and the active region? This is a lower index region that results in a leaky mode behavior. Can this be finessed to further improve the detectivity? Our estimates indicate that close to 100% quantum efficiency can be achieved, dramatically improving the performance of QD photodetectors which have a deserved stigma of low QE. What is the optimal strategy for incorporating high absorption detectors such as strained layer superlattices? At first blush, it would seem that the best strategy is to reduce the superlattice thickness so that the combination has a high quantum efficiency, but at a reduced dark current due to the reduced active volume. What about the rest of the structure, the back contact and the remaining substrate? Clearly an overall optimization based on modeling and understanding the complex modal structure of the entire device is required.

Plasmonic Arrays and Integration into Focal Planes In

this program, we have successfully demonstrated the first fully integrated plasmonics-coupled focal plane array.⁹ Fig. 2 shows the structure (with 25 μm pixels). The important

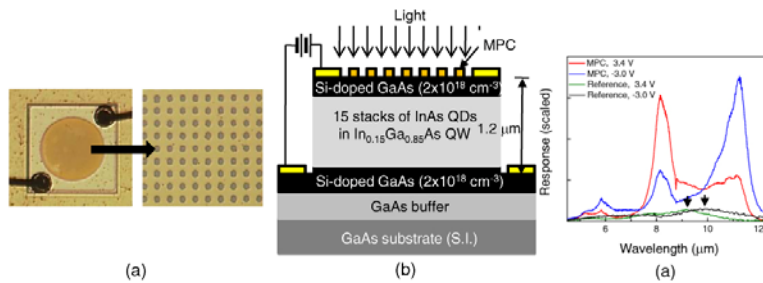


Fig. 1: (a) Top down view of detector showing plasmonic structure and contacts. (b) Cross section of plasmonics detector showing epitaxial detail; (c) Enhanced detectivity of the plasmonic detector compared to a bare reference for two bias polarities. The two peaks correspond to the (1,0) and (1,1) plasmon resonances. The two black arrows point to the peaks of the bare detector response for the same biases. The 30 \times detectivity improvement is evident.

physics is to understand the interaction between the plasma wave attenuation (which is 100s of μm s in the IR) and the infrared absorption in the semiconductor. The goal is to maximize the quantum efficiency by absorbing the majority of the radiation within the 25- μm pixel width. We have demonstrated that a corrugated metal surface that can be patterned and deposited after the growth on the top surface of the epitaxy can be used for the SPW coupling. This vastly simplifies the process of integrating the plasmonics structure with standard FPA flip-chip manufacturing processes for integration with a ROIC.

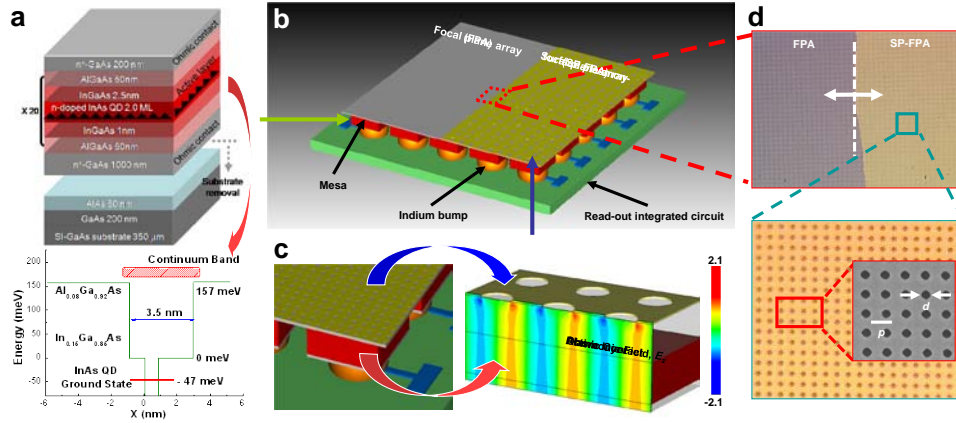


Figure 2: a) Detail of the epitaxial structure and band diagram; b) schematic view of the focal plane array showing the separation between bare and MPC regions and the bump bonding to the ROIC; c) simulation of the enhanced SPW fields; d) enlarged views of the MPC including a SEM of the detailed pattern.

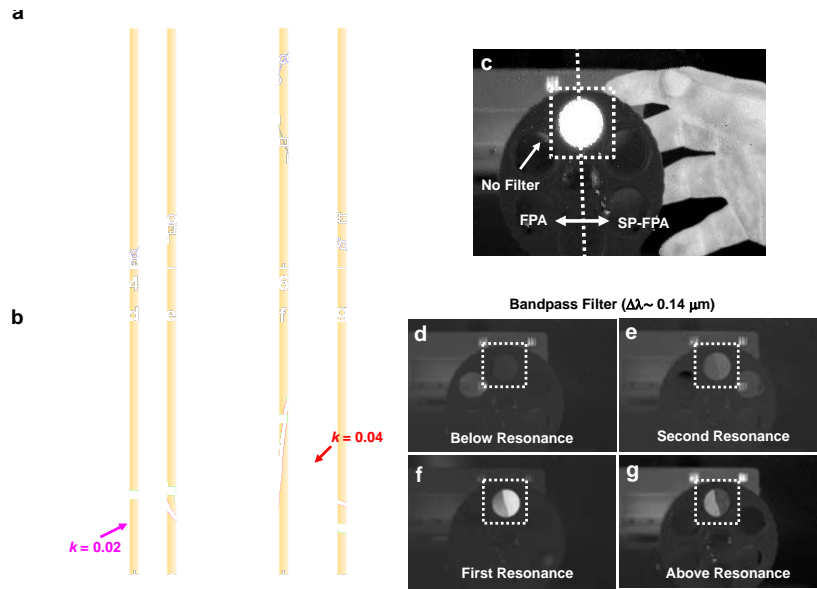


Fig. 3: (a) Spectral response of the two halves of the FPA. (b) Difference (plasmonic-bare) and fit of (1,0) and (1,1) resonances. (c) Image from the FPA with a black body behind the open aperture. (d-g) Images with different filters (see (a-b) for spectral identification, clearly showing enhancement/depletion from the plasmonic coupling.

Towards a bioinspired infrared retina The most exciting new scientific application of this technology is to encode different spectral and polarization information in each pixel of the FPA. The SPW coupling dimensions are large in the infrared, $\sim \lambda/n$, where λ is the wavelength of interest and n the semiconductor refractive index, well within the capabilities of standard lithogra-

phy systems. It is worth noting that the human eye is not a continuous spectroscopic instrument, but rather encodes color information in the relative intensities of three broadband and largely overlapping spectral sensors. Clearly, nature has judged that a simple linear coding across wavelengths is not the most efficient strategy! There is quite a bit of flexibility in the design of the coupling structure (both the metal film and the semiconductor layer structure) that will allow a vigorous investigation of alternatives across a broad range of bandwidths, coupling strengths, SPW absorption/scattering lengths and spectral overlaps.

-
- ¹ G. Vane and A.FH. Goetz, *Terrestrial imaging spectroscopy*, Remote Sens. Environ. **47**(4), 1-29 (1988).
 - ² J. P. Kerekes, M.K. Griffin, J.E. Baum and K.E. Farrar, Modeling of LWIR hyperspectral system performance for surface object and effluent detection applications, Proc. SPIE **4381**, 348-359 (2001).
 - ³ D. Manolakis and G.A. Shaw, *Detection algorithms for hyperspectral imaging applications*, IEEE Signal Proc. Mag. **19**(1), 29-43 (2002).
 - ⁴ L. Hutchinson, Imaging: Digital infrared breast scan shows promise for detecting cancer. Nature Review Clinical Oncology **7**, 483 (2010).
 - ⁵ SEEING PHOTONS: Progress and Limits of Visible and Infrared Sensor Arrays, **S.R.J. Brueck**, committee chair, National Academy Press, 2010 isbn: 978-0-309-15304-1
 - ⁶ A. V. Barve, S. J. Lee, S. K. Noh, and **S. Krishna**, *Review of current progress in quantum dot infrared photodetectors*, Laser & Photon. Rev. 1–13 (2009) (invited review).
 - ⁷ For a recent review, see: F.J. Garcia-Vidal, L. Martin-Moreno, T.W. Ebbesen and L. Kuipers, *Light passing through subwavelength apertures*, Rev. of Mod. Phys. **82**, 729-787 (2011).
 - ⁸ S.C. Lee, **S. Krishna** and **S.R.J. Brueck**, *Quantum dot infrared photodetector enhanced by surface plasma wave excitation*, Opt. Express **17**(25), 23160-23168 (2009).
 - ⁹ S.J. Lee, Z. Ku, A. Barve, J. Montoya, W-Y. Jang, **S.R.J. Brueck**, M. Sundaram, A. Reisinger, **S. Krishna** and S. K. Noh, *A Monolithically Integrated Plasmonic Infrared Quantum Dot Camera*, Nature Commun. **2**, 286 (2011).

14. 3D Interferometric Lithography (Brueck)

Chiral, coil-spring-like helical photonic crystal structures are useful for optical applications including: circular polarizers, optical diodes, and optical isolators.^{1,2} A chiral material lacks any planes of mirror symmetry and is characterized by a cross coupling between the electric and the magnetic material response. This results in breaking the degeneracy between the two circularly polarized waves; i.e., the refractive index is increased for one circular polarization and reduced for the other. This gives rise to interesting phenomena that are not available from conventional materials including the possibility of a negative refractive index for one circular polarization while the other remains positive.³

Traditionally, helical structures have been formed using glancing angle deposition (GLAD), a technique based on physical vapor deposition that employs oblique angle deposition conditions, or serial direct laser writing based on multiphoton absorption.^{4,5} Both of these techniques are slow processes. GLAD runs into shadowing and uniformity issues across large areas, and direct laser writing is impractical for fabricating helical structures over large areas.

A novel technique has been developed in this program that creates dense arrays of helical structures (3D photonic crystals) using a simple, parallel, large-area lithography process with the capability to regulate the size, shape, and periodicities of the crystal, allowing independent control over the helical lattice periodicity and coil pitch of the 3D PhC. This technique consists of a simple two-beam off-axis Michelson interferometric lithography arrangement with multiple exposures followed by a single development step.⁶

Interferometric lithography (IL) can produce gratings down to a $\lambda/4n$ half-pitch.⁷ IL also has a large depth-of-focus with inherent uniformity for forming large-area gratings on photoresist-coated wafers. Most important of all there is no need to use a mask, or focusing optical system, to produce very small pitch structures. This provides inexpensive large-area fabrication capabilities for nm-scale pitch periodic features. Using an off-axis Michelson interferometric technique producing helical structures over large area is rapid in comparison to previously demonstrated techniques. The helical pillar photoresist structures are very prone to collapse during the drying step of the development process due to the surface tension applied to the high aspect ratio and small substrate contact area of the photoresist. The inverse structures, helical holes, can be obtained by lowering the exposure dose, and will not have any issues with pattern collapse. These helical holes can subsequently be used as a mandrel for a sol-gel or metal electroforming process, enabling a high index contrast chiral metamaterial. In this initial demonstration, we concentrated on the helical pillars.

A mathematical model of the 3D PhCs available by this new 3D IL approach has been derived. These models are used to generate helical three-dimensional PhCs figures that are then compared to experimentally produced helical PhCs. The experimentally produced helical PhCs are then evaluated by their impact on linearly polarized light. Measurements of the transmitted light for

various polarizations were recorded, and a plot of the degree-of-polarization from several measurements is presented.

Traditionally three-dimensional IL has involved a single exposure with multiple (four or more) plane waves. However, multiple-exposure, two-beam IL can also be used to create a 3D pattern.⁸

To better understand these relationships and the parameter space for the z -period compared to the transverse periods, a plot of available z -periods versus available (x , y) periods for an exposure wavelength of $\lambda=355$ nm and photoresist index of refraction $n_r=1.3$, is presented in Fig. 1. In this plot, the red (solid line at $\sim 20^\circ$ to the vertical) line represents the locus for the z -period versus the x -period for on-axis multi-beam 3D IL PCs. The cyan colored area represents the much greater range of combinations of z -periods versus x -periods achievable with off-axis multiple-exposure 3D IL PhCs. The green dashed line (at $\sim 45^\circ$) represents the symmetrical PC (z -period = x -period). As the refractive index of the photoresist increases, to more realistic values of ~ 1.7 – 1.8 , the area of achievable pitches (light cyan colored area) decreases due to the reduction of the available beam angles in the resist. However, for immersion approaches the relevant parameter is $n_{PR}/n_{fluid} \sim 1.7/1.4 \sim 1.3$, restoring the wide range of accessible periods for practical photoresists.

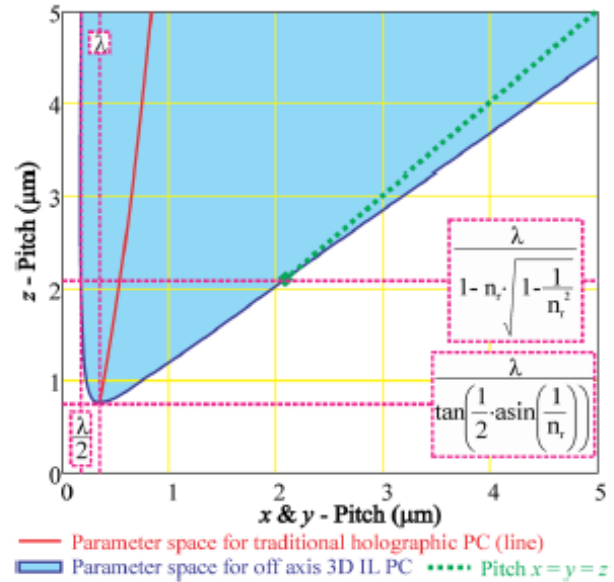


Fig. 1: 3D IL accessible parameter space ($\lambda = 355$ nm; $n_{pr}/n = 1.3$)

Both images created by mathematical models and SEM images of the experimental 3D PCs using the multiple exposure IL setup are presented. The set of exposures were made using a six-exposure process (with 60° rotations and $\pi/3$ phase-shift in the z -plane between each exposure) that creates a 3D helical PC. The experimental PCs are made in Futurrex NR7-6000P negative photoresist at a thickness of $5 \mu\text{m}$ exposed at 355 nm. In Fig. 2, mathematically simulated images and experimental SEM images are shown side by side. The result is an array of helical spirals that have a 1926 nm period along the z -axis, and are spaced apart by 1102 nm on a hexagonal grid. The silicon wafer substrates of the experimental PCs are cleaved for cross-section SEMs. The PC is very uniform over the $10\text{-}\mu\text{m}^2$ area imaged; the overall area of the PC was 2 cm^2 . Any variation in the photonic crystal coil size is likely due to variations in exposure dose versus photoresist depth resulting from light absorption in the photoresist, and to a smaller extent from developer diffusion and concentration fluctuations. The coil sizes in the crystal structure vary

slightly from edge to edge of the 2 cm^2 PC mostly due to exposure variations. For the top-down SEM images in Fig. 7, one full rotation of the crystal coils is visible. The top down SEM clearly shows the hexagonal symmetry of the helical crystals. Optical measurements have been reported elsewhere.

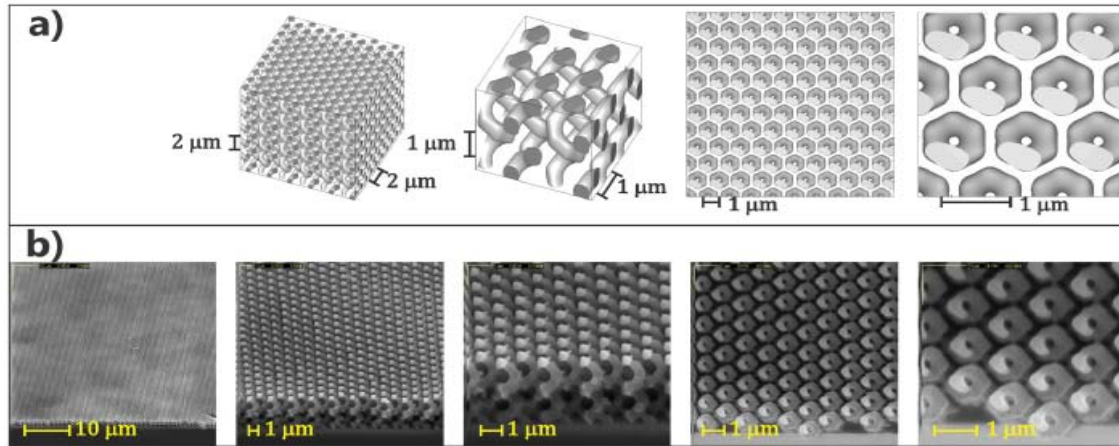


Fig. 2: Helical PCs made using six exposures with 60° rotation. a) simulations; b) SEM images of experimental structures.

-
- ¹ J. K. Gansel, M. Wegener, S. Burger, and S. Linden, *Opt. Express* **18**, 1059 (2010).
 - ² J. K. Gansel, M. Thiel, M. S. Rill, M. Decker, K. Bade, V. Saile, G. von Freymann, S. Linden, and M. Wegener, *Science* **325**, 1513 (2009).
 - ³ S. Zhang, Y.-S. Park, J. Li, X. Lu, W. Zhang, and X. Zhang, *Phys. Rev. Lett.* **102**, 23901 (2009).
 - ⁴ Y. J. Park, K. M. A. Sobahan, and C. K. n Hwangbo, *Opt. Express* **16**, 5186 (2008).
 - ⁵ M. Thiel, H. Fischer, G. von Freymann, and M. Wegener, *Opt. Lett.* **35**, 166 (2010).
 - ⁶ A. K. Raub, "Large Area 3D Photonic Crystals with Embedded Waveguides," Ph.D. Dissertation, UNM, 2010, <http://hdl.handle.net/1928/12108>.
 - ⁷ S. H. Zaidi and S. R. J. Brueck, *J. Vac. Sci. Technol.* **B 11**, 658 (1993).
 - ⁸ A. K. Raub and S. R. J. Brueck, *J. Vac. Sci. Technol.* **B 28**, C6O38 (2010).

2009 PUBLICATIONS

S.D. Hersee, M. Fairchild, A.K. Rishinaramangalam, M.S. Ferdous, L. Zhang, P.M. Varangis, B.S. Swartzentruber and A.A. Talin, [GaN nanowire light emitting diodes based on templated and scalable nanowire growth process](#), Electron. Lett. **45**, 75-76 (2009)

A. A. Talin, B. S. Schwartzentruber, François Léonard, X. Wang and S. D. Hersee, [Electrical transport in GaN nanowires grown by selective epitaxy](#), Jour. Vac. Sci. Technol. **B27**, 2040-2043 (2009).

I. Arslan, J. K. Hyun, R. Emi, M. N. Fairchild, S. D. Hersee and D. A. Muller, [Using electrons as a high-resolution probe of optical modes in individual nanowires](#), Nano Lett. **9**, 4073-4077 (2009).

F. Grillot, N. A. Naderi, M. Pochet, C.-Y. Lin, P. Besnard and L. F. Lester, [Tuning of the critical feedback level in 1.55- \$\mu\$ m quantum dash semiconductor laser diodes](#), IET Optoelectron. **3**, 242,247 (2009).

L. Wang and R. K. Jain, [Maximization of nonlinear fluorescence from ultrasmall \(\$< 2\$ nm\) semiconductor quantum dots to be used for deep tissue imaging](#), J. Opt. Soc. Am. **B26**, 2161-2166 (2009).

Zahyun Ku, Jingyu Zhang and S. R. J. Brueck, [Bi-anisotropy of multiple-layer fishnet negative-index metamaterials due to angled sidewalls](#), Optics Express **17**, 6782-6789 (2009).

Zahyun Ku and S. R. J. Brueck, [Experimental Demonstration of Sidewall-Angle Induced Bi-Anisotropy in Multiple-Layer Negative-Index Metamaterials](#), Appl. Phys. Lett. **94**, 153107 (2009).

S. C. Lee and S. R. J. Brueck, [Scaling of the surface migration length in nanoscale patterned growth](#), Appl. Phys. Lett. **94**, 153110 (2009).

Liang Xue, S. R. J. Brueck and R. Kaspi, [Widely Tunable Distributed Feedback Lasers with Chirped Gratings](#), Appl. Phys. Lett. **94**, 161102 (2009).

S. C. Lee, Z. Ku, W.-Y. Jang, J. H. Kim, C. Hains, S. Krishna and S. R. J. Brueck, [Mid-Infrared Transmission through a Subwavelength Circular Aperture Coupled to a Surrounding Concentric Metal Grating by Surface Plasmon Excitation](#), Phys. Stat. Sol. **C6**, S175-S178 (2009).

S. C. Lee, E. Pils, S. Krishna and S. R. J. Brueck, [Mid-Infrared Transmission Enhancement through a Subwavelength Metal Hole Array with an Impedance Matching Dielectric Layer](#), Electron. Lett. **45**, 643-645 (2009).

K. M. Dani, Zahyun Ku, Prashanth C. Upadhy, Rohit P. Pransankumar, S. R. J. Brueck and Antoinette J. Taylor, [Sub-Picosecond Optical Switching with a Negative Index Metamaterial](#), Nano Lett. **9**, 3565-3569 (2009).

Zahyun Ku, K. M. Dani, P. C. Upadhy, and S. R. J. Brueck, [Bi-Anisotropic Negative-Index, Metamaterial Embedded in a Symmetric Medium](#), Jour. Opt. Soc. Amer. **B26**, 34-38 (2009).

D. B. Burckel, C. M. Washburn, A. K. Raub, S. R. J. Brueck, D. R. Wheeler, S. M. Brozik and R. Polsky, [Lithographically defined porous carbon electrodes](#), Small **5**, 2792-2796 (2009).

S. C. Lee, S. Krishna and S. R. J. Brueck, [Quantum Dot Infrared Photodetector Enhanced by Surface Plasma Wave Excitation](#), Optics Exp. **17**, 23161 (2009).

J. Tatebayashi, A. Jallipalli, M. N. Kutty, S. Huang, K. Nunna, G. Balakrishnan, L. Ralph Dawson, and D. L. Huffaker, [Monolithically Integrated III-Sb-Based Laser Diodes Grown on Miscut Si Substrates \(invited\)](#), IEEE Jour. Sel. Top. in Quantum Electron. **15**, 716-723 (2009).

A. Jallipalli, G. Balakrishnan, S. H. Huang, T. J. Rotter, K. Nunna, B. L. Liang, L. R. Dawson, and D. L. Huffaker, [Structural Analysis of Highly Relaxed GaSb Grown on GaAs Substrates with Periodic Interfacial Array of 90° Misfit Dislocations](#), Nanoscale Res. Lett. **4**, 1458-1462 (2009).

A. Jallipalli, K. Nunna, M. N. Kutty, G. Balakrishnan, G. B. Lush, L. R. Dawson, and D. L. Huffaker, [Compensation of interfacial states located inside the “buffer-free” GaSb/GaAs \(001\) heterojunction via \$\delta\$ -doping](#), Appl. Phys. Lett. **95**, 072109 (2009).

J. M. Yarborough, Y.-Y. Lai, Y. Kaneda, J. Hader, J. V. Moloney, T. J. Rotter, G. Balakrishnan, C. Hains, D. Huffaker, S. W. Koch, and R. Bedford, [Record pulsed power demonstration of a 2 \$\mu\$ m GaSb-based optically pumped semiconductor laser grown lattice-mismatched on an AlAs/GaAs Bragg mirror and substrate](#), Appl. Phys. Lett. **95**, 081112 (2009).

T. J. Rotter, J. Tatebayashi, P. Senanayake, G. Balakrishnan, M. Rattunde, J. Wagner, J. Hader, J. V. Moloney, S. W. Koch, L. R. Dawson, and D. L. Huffaker, [Continuous-Wave, Room-Temperature Operation of 2- \$\mu\$ m Sb-Based Optically-Pumped Vertical-External-Cavity Surface-Emitting Laser Monolithically Grown on GaAs Substrates](#), Appl. Phys. Exp. **2**, 112102 (2009).

A. Jallipalli, K. Nunna, M. N. Kutty, G. Balakrishnan, L. R. Dawson, and D. L. Huffaker, [Electronic characteristics of the interfacial states embedded in “buffer-free” GaSb/GaAs \(001\) heterojunctions](#), Appl. Phys. Lett. **95**, 202107 (2009).

2010 PUBLICATIONS

- A. A. Talin, F. Leonard, A. M. Katzenmeyer, B. S. Swartzentruber, S. T. Picraux, M. E. Toimil-Molares, J. G. Cederberg, X. Wang, S. D. Hersee and A. Rishinaramangalum, [*Transport characterization in nanowires using an electrical nanoprobe*](#), Semicond. Sci. Technol. **25**, 024015 (2010).
- F. Liu and M. Hossein-Zadeh, [*On the performance of high-Q multiring optical filters*](#), IEEE Photon. Jour. **2**, 991-1002 (2010).
- M. Hossein-Zadeh and K. J. Vahala, [*An optomechanical oscillator on a silicon chip*](#), IEEE Jour. Sel. Top. in Quant. Electron. **16**, 276-287 (2010).
- N. A. Naderi, F. Grillot, K. Yang, J. B. Wright, A. Gin, and L. F. Lester, [*Two-color multi-section quantum dot distributed feedback laser*](#), Opt. Exp. **18**, 27028-27035 (2010).
- D. Xia, X. He, Y.-B. Jiang, G. P. Lopez and S. R. J. Brueck, [*Tailoring Anisotropic Wetting Properties on Submicrometer-Scale Periodic Grooved Surfaces*](#), Langmuir **26**, 2700 (2010).
- S. C. Lee, S. Krishna and S. R. J. Brueck, [*Light Direction Dependent Plasmonic Enhancement in Quantum Dot Infrared Photodetectors*](#), Appl. Phys. Lett. **97**, 021112 (2010).
- J. Adams, G. Tizazu, S. Janusz, S. R. J. Brueck, G. P. Lopez and G. J. Leggett, [*Large-Area Nanopatterning of Self-Assembled Monolayers of Alkanethiolates by Interferometric Lithography*](#), Langmuir **26**, 13600-13606 (2010).
- S. Smolev, Z. Ku, S. R. J. Brueck, I. Brener, M. B. Sinclair, G. A. Ten Eyck, W. L. Langston, and L. I. Basilio, [*Resonant coupling to a dipole absorber inside a metamaterial: Anticrossing of the negative index response*](#), J. Vac. Sci. Technol. **B28**, C6016 (2010).
- D. Xia, Y-B Jiang, X. He and S. R. J. Brueck, [*Titania Nanostructure Arrays from Lithographically Defined Templates*](#), Appl. Phys. Lett. **97**, 223106 (2010).
- A. K. Raub and S. R. J. Brueck, [*Large Area 3D Photonic Crystals with Embedded Waveguides*](#), Jour. Vac. Sci. Technol. **B28**, C6038 (2010).
- Y. Tawk, A. R. Albrecht, S. Hemmady, G. Balakrishnan, and C. G. Christodoulou, [*Optically Pumped Frequency Reconfigurable Antenna Design*](#), IEEE Antennas and Wireless Prop. Lett. **9**, 280-283 (2010).
- Y.-Y. Lai, J. M. Yarborough, Y. Kaneda, J. Hader, J. V. Moloney, T. J. Rotter, G. Balakrishnan, C. Hains, and S. W. Koch, [*340-W Peak Power From a GaSb 2- \$\mu\$ m Optically Pumped Semiconductor Laser \(OPSL\) Grown Mismatched on GaAs*](#), IEEE Photon. Tech. Lett. **22**, 1253-1255 (2010).

A.R. Albrecht, T.J. Rotter, C.P. Hains, A. Stintz, J.V. Moloney, K.J. Malloy and G. Balakrishnan, [*Multi-watt 1.25 \$\mu\text{m}\$ quantum dot VECSEL*](#), *Electron. Lett.* **46**, 856-857 (2010).

E. Plis, J. B. Rodriguez, G. Balakrishnan, Y. D. Sharma, H. S. Kim, T. Rotter and S. Krishna, [*Mid-infrared InAs/GaSb strained layer superlattice detectors with nBn design grown on a GaAs substrate*](#), *Semicon. Sci. and Tech.* **25**, 085010 (2010).

2011 PUBLICATIONS

S. D. Hersee, A. K. Rishinaramangalam, M. N. Fairchild, L. Zhang, and P. Varangis, [*Threading defect elimination in GaN nanowires*](#), Jour. Matl. Res. **26**, 2293-2298 (2011).

N. J. Withers, H. Cao, G. A. Smolyakov and M. Osinski, [*Highly unidirectional Y-junction-coupled S-section quantum-dot ring lasers*](#), Appl. Phys. Lett. **99**, 231103 (2011).

F. Grillot, N. A. Naderi, J. B. Wright, R. Rahunathan, M. T. Crowley and L. F. Lester, [*A dual-mode quantum dot laser operating in the excited state*](#), Appl. Phys. Lett. **99**, 231110 (2011).

G. A. Smolyakov and M. Osinski, [*High-speed modulation analysis of strongly injection-locked semiconductor ring lasers*](#), IEEE Jour. of Quan. Electron. **47**, 1463-1471 (2011).

S. Lan and M. Hossein-Zadeh, [*Faraday effect in high-Q whispering-gallery mode optical cavities*](#), IEEE Photon. Jour. **3**, 872-880 (2011).

M. Hossein-Zadeh and A. F. J. Levi, [*Ring resonator based photonic microwave receiver modulator with picowatt sensitivity*](#), IET Optoelectron. **5**, 36-39 (2011).

M. Klopfer and R. K. Jain, [*Plasmonic quantum dots for nonlinear optical applications \(invited\)*](#), Opt. Matl. Exp. **1**, 1353-1366 (2011).

Keshav M. Dani, Zahyun Ku, Prashanth C. Upadhyay, Rohit P. Prasankumar, Antoinette J. Taylor, and S. R. J. Brueck, [*Ultrafast nonlinear optical spectroscopy of a dual-band negative index metamaterial all-optical switching device*](#), Opt. Exp. **19**, 3973 (2011).

Deying Xia, Zahyun Ku, S. C. Lee and S. R. J. Brueck, [*Nanostructures and Functional Materials Fabricated by Interferometric Lithography \(review\)*](#), Adv. Materials **23**, 147-179 (2011).

W. Pan, J. L. Reno, D. Li and S. R. J. Brueck, [*Quantum Hall Ferromagnetism in the Presence of Tunable Disorder*](#), Phys. Rev. Lett. **106**, 156806 (2011).

S.J. Lee, Z. Ku, A. Barve, J. Montoya, W-Y. Jang, S.R.J. Brueck M. Sundaram, A. Reisinger, S. Krishna and S. K. Noh, [*A Monolithically Integrated Plasmonic Infrared Quantum Dot Camera*](#), Nature Comm. **2**, 263 (2011).

Jingyu Zhang, Li Wang, S. Krishna, M. Sheik-Bahae and S. R. J. Brueck, [*Saturation of the Second Harmonic Generation from GaAs Filled Metallic Hole Arrays by Nonlinear Absorption*](#), Phys. Rev. **B83**, 165438 (2011).

Getachew Tizazu, Osama El-Zubir, Steven R. J. Brueck, David G. Lidzey, Graham J. Leggett and Gabriel P. Lopez, [*Large Area Nanopatterning of Alkylphosphonate Self-Assembled Mono-*](#)

[*layers on Titanium Oxide Surfaces by Interferometric Lithography*](#), *Nanoscale* (Royal Society) **3**, 2511-2516 (2011).

S. C. Lee, S. Krishna and S. R. J. Brueck, [*Plasmonics-Enhanced Photodetectors for Focal Plane Arrays*](#), *IEEE Photon. Tech. Lett.* **23**, 935-937 (2011).

S. C. Lee, L. R. Dawson, S. H. Huang and S.R.J. Brueck, [*Lithography-free nanoscale patterned growth of GaAs on Si\(001\) with sub-100-nm silica nanoparticles by molecular beam epitaxy*](#), *Crystal Growth and Design* **11**, 3673-3676 (2011).

A. K. Raub and S.R.J. Brueck, [*Large-Area 3D Helical Photonic Crystals*](#), *J. Vac. Sci. Technol.* **B29**, 06FF02 (2011).

A. R. Albrecht, A. Stintz, F. T. Jaeckel, T. J. Rotter, P. Ahirwar, V. J. Patel, C. P. Hains, Luke F. Lester, Kevin J. Malloy and Ganesh Balakrishnan, [*1220–1280-nm optically pumped InAs quantum dot-based vertical external-cavity surface-emitting laser*](#), *IEEE Jour. Sel. Top. in Quantum Electron.* **17**, 1787-1793 (2011).

S.P.R. Clark, P. Ahirwar, F. T. Jaeckel, C. P. Hains, A. R. Albrecht, T. J. Rotter, L. R. Dawson, G. Balakrishnan, P. E. Hopkins, L. M. Phinney, J. Hader and J. V. Moloney, [*Growth and thermal conductivity analysis of polycrystalline GaAs on chemical vapor deposition diamond for use in thermal management of high-power semiconductor lasers*](#), *J. Vac. Sci. Technol.* **B29**, 03C130 (2011).

A. R. Albrecht, C. P. Hains, T. J. Rotter, A. Stintz, K. J. Malloy, and G. Balakrishnan, [*High power 1.25 \$\mu\text{m}\$ InAs quantum dot vertical external-cavity surface-emitting laser*](#), *J. Vac. Sci. Technol.* **B29**, 03C113 (2011).

P. Ahirwar, S. P.R. Clark, V. Patel, T. J. Rotter, C. Hains, A. Albrecht, L. R. Dawson, and G. Balakrishnan, [*Perforated \(In\)GaSb quantum wells on GaSb substrates through the use of As₂ based in situ etches*](#), *J. Vac. Sci. Technol.* **B29**, 04I204 (2011).

P. E. Hopkins, J. C. Duda, S. P. Clark, C. P. Hains, T. J. Rotter, L. M. Phinney, and G. Balakrishnan, [*Effect of dislocation density on thermal boundary conductance across GaSb/GaAs interfaces*](#), *Appl. Phys. Lett.* **98**, 161913 (2011).

S. Huang, G. Balakrishnan, and D. L. Huffaker, [*Growth Mode and Defect Evaluation of GaSb on GaAs Substrate: A Transmission Electron Microscopy Study*](#), *J. Nanosci. and Nanotech.* **11**, 1-6 (2011).

U. S. PATENT APPLICATIONS

Three patent applications, two provisional and one utility, were filed during the course of this contract. Details are provided below.

STC.UNM	US Patent Applic.	Status	Title	Inventors	Date Filed
2010-003-02	US10/53553	Pat. Pend.	Plasmonic Detectors	S.R.J. Brueck, S. C. Lee, S. Krishna	10/21/2010
2011-042-02	61/439,722	Provisional	Large Area 3D Photonic Crystals with Embedded Waveguides	S.R.J. Brueck, A. K. Raub	2/5/2011
2012-024	61/546,326	Provisional	Multilayered Plasmonic Quantum Dot	R. Jain, M. Kloper	10/12/2011

In addition, one patent acknowledging support from a prior AFOSR award was issued during the period of this grant.

US 7,968,359 [Thin-Walled Structures](#), Stephen D. Hersee, issued June 28, 2011.